The Astrophysical Journal, 796:59 (11pp), 2014 November 20 doi:10.1088/0004-637X/796/1/59

H I, CO, AND *PLANCK*/*IRAS* DUST PROPERTIES IN THE HIGH LATITUDE CLOUD COMPLEX, MBM 53, 54, 55 AND HLCG 92−35. POSSIBLE EVIDENCE FOR AN OPTICALLY THICK H I ENVELOPE AROUND THE CO CLOUDS

Yasuo Fukui[1], Ryuji Okamoto[1], Ryohei Kaji[1], Hiroaki Yamamoto[1], Kazufumi Torii[1], Takahiro Hayakawa[1], Kengo Tachihara[1], John M. Dickey[2], Takeshi Okuda[1,3], Akio Ohama[1], Yutaka Kuroda[1], and Toshihisa Kuwahara[1]
[1] Department of Physics, Nagoya University, Chikusa-ku, Nagoya 464-8602, Japan; fukui@a.phys.nagoya-u.ac.jp
[2] University of Tasmania, School of Maths and Physics, Private Bag 37, Hobart, TAS 7001, Australia
[3] National Astronomical Observatory of Japan, 2-21-1 Osawa, Mitaka, Tokyo 181-8588, Japan
Received 2014 January 28; accepted 2014 September 22; published 2014 November 5

ABSTRACT

We present an analysis of the H I and CO gas in conjunction with the *Planck*/*IRAS* submillimeter/far-infrared dust properties toward the most outstanding high latitude clouds MBM 53, 54, 55 and HLCG 92−35 at $b = -30^\circ$ to -45°. The CO emission, dust opacity at 353 GHz (τ_{353}), and dust temperature ($T_{\rm d}$) show generally good spatial correspondence. On the other hand, the correspondence between the H I emission and the dust properties is less clear than in CO. The integrated H I intensity $W_{\rm H\,I}$ and τ_{353} show a large scatter with a correlation coefficient of ∼0.6 for a $T_{\rm d}$ range from 16 K to 22 K. We find, however, that $W_{\rm H\,I}$ and τ_{353} show better correlation for smaller ranges of $T_{\rm d}$ every 0.5 K, generally with a correlation coefficient of 0.7–0.9. We set up a hypothesis that the H I gas associated with the highest $T_{\rm d} \geqslant 21.5$ K is optically thin, whereas the H I emission is generally optically thick for $T_{\rm d}$ lower than 21.5 K. We have determined a relationship for the optically thin H I gas between atomic hydrogen column density and τ_{353}, $N_{\rm H\,I}\,({\rm cm}^{-2}) = (1.5 \times 10^{26}) \cdot \tau_{353}$, under the assumption that the dust properties are uniform and we have applied this to estimate $N_{\rm H\,I}$ from τ_{353} for the whole cloud. $N_{\rm H\,I}$ was then used to solve for $T_{\rm s}$ and $\tau_{\rm H\,I}$ over the region. The result shows that the H I is dominated by optically thick gas having a low spin temperature of 20–40 K and a density of 40–160 cm^{-3}. The H I envelope has a total mass of $\sim 1.2 \times 10^4\ M_\odot$, an order of magnitude larger than that of the CO clouds. The H I envelope properties derived by this method do not rule out a mixture of H I and H_2 in the dark gas, but we present indirect evidence that most of the gas mass is in the atomic state.

Key words: ISM: clouds – ISM: individual objects (MBM 53, 54, 55 and HLCG 92-35) – radio lines: ISM

Online-only material: color figures

1. INTRODUCTION

The neutral interstellar medium (ISM) consists of H I, H_2, and possibly "dark gas," which is believed to be undetectable in line emission of H I or CO (Grenier et al. 2005; *Planck* Collaboration et al. 2011b). The H I emission at a 21 cm wavelength and the CO emission at 2.6 mm offer tools for probing atomic and molecular hydrogen. The CO clouds have a low kinetic temperature of 10–100 K with a density above 1000 cm^{-3} as derived by analyses of multi-*J* CO transitions (e.g., Castets et al. 1990). The CO intensity is converted into molecular column density by an $X_{\rm CO}$ factor, which is empirically determined by assuming dynamical equilibrium of the CO clouds, dust properties measured in extinction and/or far-infrared emission, and comparison with gamma rays created by proton–proton collisions via neutral pion decay (e.g., Blitz et al. 2007; Fukui & Kawamura 2010; Bolatto et al. 2013). On the other hand, the physical parameters of the H I gas have been rather ambiguous, mainly because the H I emission has a single observed quantity, intensity as a function of velocity, for two independent variables, spin temperature $T_{\rm s}$ and H I optical depth $\tau_{\rm H\,I}$, which does not allow us to determine each of these observationally. The H I consists of warm and cold components (for a review see Kalberla & Kerp 2009; Dickey & Lockman 1990). The mass of the H I gas having a spin temperature higher than ∼100 K is measurable at reasonably high accuracy under an optically thin approximation, while the cold component, having a spin temperature of 20–80 K is measured by comparing the absorption and emission H I profiles only where background continuum sources are available (Dickey et al. 2003; Heiles & Troland 2003). It is notable that some recent works on TeV gamma-ray supernova remnants show that the cold H I gas which is not detectable in CO at a 1σ integrated intensity level of ∼1 K km s^{-1} (Fukui et al. 2012) is responsible for the gamma-rays via collision between cosmic-ray protons and interstellar protons (Fukui et al. 2012; Fukui 2013; Fukuda et al. 2014). However, the observed sample of cold H I is limited and further efforts are still needed to better constrain the physical properties of cold H I.

Recent progress in measuring the infrared and submillimeter emission over the whole sky has been remarkable. These observations are strongly motivated by the aim to precisely measure the cosmic microwave background (CMB) radiation and its polarization. In particular, the *Planck* collaboration released a whole sky distribution of dust temperature $T_{\rm d}$ and dust opacity τ_{353} at 5 arcmin resolution which was achieved through sensitive measurements of the dust emission above 100 GHz in the Galactic foreground. Five papers by the *Planck* collaboration presented comparisons between CO and dust emission (*Planck* Collaboration et al. 2011b, 2011c, 2011d, 2011e, 2011f). These studies derived basic physical relationships between neutral gas and dust emission and concluded that dark gas (Grenier et al. 2005) occupies 15% of the ISM, where the H I emission is assumed to be optically thin. Similar studies on 21 cm H I emission include Lee et al. (2012) and *Planck* Collaboration et al. (2011a).

The high latitude molecular clouds MBM 53, 54, 55 and HLCG 92−35 are one of the largest cloud systems in the sky at a Galactic latitude of -30° to -45° with only minor

background components (Magnani et al. 1985). The distance of the cloud system is determined to be 150 pc (Welty et al. 1989). Yamamoto et al. (2003) used the NANTEN 4 m telescope to observe $J = 1$–0 transitions of ^{12}CO, ^{13}CO, and C^{18}O and mapped the molecular distribution. The velocity of the MBM 53, 54, 55 and HLCG 92−35 clouds is mainly in the range from -11 km s^{-1} to 0 km s^{-1} for CO. The half-power beam widths were 2.6–2.7 arcmin and their grid spacings were 4 or 8 arcmin for ^{12}CO and 2 arcmin for ^{13}CO and C^{18}O. They also identified associated H I gas at 36 arcmin resolution and discussed that the H I gas is being converted into H_2 under the dynamical effect of a nearby shell driven by stellar winds. Gir et al. (1994) studied and identified the associated H I, while their coverage was limited to ∼1/2 of the area studied by Yamamoto et al. (2003). For reference, this region is rich in high latitude clouds including a far-infrared looplike structure in Pegasus; Yamamoto et al. (2006) observed this loop in CO ($J = 1$–0) lines. MBM 53, 54, 55 and HLCG 92−35 clouds show no sign of active star formation and are an ideal target for studying detailed ISM properties under the general interstellar radiation field (ISRF). The regions of the MBM 53, 54, 55 and HLCG 92−35 clouds and the Pegasus loop have also been used to test CO component separation in analysis of the CMB emission (Ichiki et al. 2014).

In order to better understand the detailed physical properties of the local ISM, we have undertaken new CO ($J = 1$–0) observations of MBM 53, 54, 55 and HLCG 92−35 with the on-the-fly (OTF) mode of the 2.6 arcmin beam of the NANTEN2 4 m telescope as part of the *N*ANTEN *S*uper *CO* survey (=NASCO), which is aiming to cover 70% of the sky. By using the H I data set at 4 arcmin resolution from the GALFA archive data, we have compared the CO and H I with the *Planck*/*IRAS* dust properties. In this paper, we present the first results from this detailed comparison. Section 2 describes the observations, Section 3 gives the results and analysis, and Section 4 presents conclusions. Another paper, which deals with the dust emission covering the whole sky, will be published separately (Fukui et al. 2014) and is complementary to the present paper.

2. OBSERVATIONAL DATASETS

In this study, we used NANTEN2 CO data, GALFA H I data, the dust emission data measured by *Planck*/*IRAS*, and the 1.4 GHz radio continuum data. All the data are gridded to 1 arcmin, smaller than the angular resolutions of these data sets.

2.1. CO Data

^{12}CO ($J = 1$–0) and ^{13}CO ($J = 1$–0) emissions were obtained by the NANTEN2 4 m millimeter/submillimeter telescope of Nagoya University, which is installed at an altitude of 4865 m in northern Chile. Observations of the ^{12}CO ($J = 1$–0) and ^{13}CO ($J = 1$–0) lines were simultaneously conducted in several sessions from 2011 November to 2013 January and cover about 75 deg^2. Only observational parameters of ^{12}CO ($J = 1$–0) are described below. The front end was a 4 K cooled Nb Superconductor–Insulator–Superconductor (SIS) mixer receiver and the double-sideband system temperature was ∼200 K including the atmosphere toward the zenith. The spectrometer was a digital Fourier transform spectrometer with 16,384 channels, providing a velocity resolution of 0.2 km s^{-1}. All observations were conducted using an OTF mapping technique with a 2.6 arcmin main beam at a 1 arcmin data sampling. Each spatial area of $1^\circ \times 1^\circ$ was mapped several times in different scanning directions to reduce scanning effects using a basket-weave technique (Emerson & Graeve 1988). These OTF data were reduced into FITS data cubes with the original IDL software. The rms noise fluctuations in ^{12}CO ($J = 1$–0) spectra after the basket-weave technique was applied were ∼1.2 K per channel in the main beam temperature, $T_{\rm mb}$. The CO data are smoothed to a 5 arcmin spatial resolution in order to be compared with the H I and *Planck*/*IRAS* data sets. The final rms noise fluctuations are ∼0.6 K per channel in a 5 arcmin smoothed beam. The pointing was checked regularly using planets and the applied corrections were always smaller than 20 arcsec. The standard sources M17 SW and Ori KL were observed for intensity calibration. The CO intensity is integrated over a velocity range of -12 km s^{-1} to +2 km s^{-1}.

2.2. H I Data

Archival data sets of the GALFA-H I survey are used (Peek et al. 2011). The survey was conducted on the Arecibo Observatory 305 m telescope and the angular resolution of the data is 4 arcmin. The rms noise fluctuations of the H I data are ∼0.25 K per channel in $T_{\rm mb}$. The H I data are also smoothed to a 5 arcmin resolution, and the rms noise fluctuations of the final H I spectra are 0.2 K per channel for the 5 arcmin beam. The H I intensity is spread over a velocity range from -49 km s^{-1} to +17 km s^{-1}, while most of the H I emission is between -25 km s^{-1} and +12 km s^{-1}.

2.3. Planck/IRAS Data

Archival data sets of the optical depth at 353 GHz (τ_{353}) and dust temperature ($T_{\rm d}$) were obtained by fitting 353, 545, and 857 GHz data of the first 15 months observed by the *Planck* satellite and 100 micron data measured by the *IRAS* satellite. Both sets of data have angular resolutions of 5 arcmin. For details, see the *Planck* Legacy Archive (PLA) explanatory supplement (*Planck* Collaboration 2013).

2.4. Radio Continuum Data

For the 1.4 GHz radio continuum background, we use the CHIPASS data (Calabretta et al. 2014) for the region at δ(J2000) $< 25^\circ$ and the data described in Reich (1982) and Reich & Reich (1986) for the region at δ(J2000) $\geqslant 25^\circ$. Their spatial resolutions are 14.4 arcmin and 35 arcmin, respectively. Although these data have lower angular resolutions than the others analyzed in the study, the peak radiation temperature of the continuum data shows small variations from ∼3.4 K to ∼4.9 K except for the area within ∼30 arcmin of the quasar 3C 454.3, which happens to be located near the CO clouds (e.g., Abdo et al. 2011). We used these lower resolution data by excluding the area around 3C 454.3.

2.5. Masking

In the present analysis, the local ISM toward the cloud system is approximated by a single layer. This is consistent with the velocity of the H I being peaked at around 0 km s^{-1}, and generally a single velocity component is dominant. In order to eliminate possible sources of contamination, we further applied the following masking. These masked areas are listed in Table 1 (see also Figure 7).

1. The areas showing CO emission higher than 1.1 K km s^{-1} (1σ) are masked in order to exclude the contribution of the CO-emitting molecular gas.

Table 1
List of Masked Areas

Position		Area	Object Name	Remark
ℓ (deg)	b (deg)	(deg^2)		
79.1	−41.8	1.1	...	[a]
81.5	−29.3	6.5	...	[a]
81.5	−33.0	6.0	...	[b]
85.6	−33.8	6.4	...	[b]
86.1	−38.2	13.1	3C 454.3	[c]
92.2	−38.9	0.3	...	[a]
98.3	−35.1	1.0	...	[a]
99.1	−41.6	13.1	...	[a]
99.4	−30.1	0.7	...	[a]
80.58	−32.47	8.5×10^{-2}	IRAS 22221+1748	Infrared source
82.42	−30.16	8.5×10^{-2}	33 Peg	Double or multiple star
83.37	−32.25	8.6×10^{-2}	Mrk 306	Galaxy
83.46	−32.39	8.6×10^{-2}	HD 213618	Star
84.67	−32.34	8.7×10^{-2}	HD 214128	Star
84.73	−32.31	8.7×10^{-2}	NGC 7316	Galaxy
86.05	−33.18	8.6×10^{-2}	Mrk 308	Seyfert galaxy
86.09	−33.57	8.6×10^{-2}	BD+19 4992	Star
87.46	−29.73	8.6×10^{-2}	NGC 7339	Radio galaxy[d]
93.53	−40.35	8.7×10^{-2}	RAFGL 3068	Variable star
93.91	−40.47	8.7×10^{-2}	NGC 7625	Interacting galaxies
97.29	−32.52	8.6×10^{-2}	IC 5298	Seyfert 2 galaxy
98.88	−36.55	8.6×10^{-2}	NGC 7678	Active galaxy nucleus
99.24	−35.40	8.6×10^{-2}	NGC 7673	Emission-line galaxy
99.32	−35.49	8.6×10^{-2}	NGC 7677	Galaxy in pair of galaxies

Notes. Columns 1 and 2 give the positions of each mask and Column 3 gives their areas. Column 4 indicates object names located at the center of each mask. Remarks on each masked area are listed in Column 5. Details on these masked areas are described in Section 2.5.

[a] The H I data is missing.

[b] There are secondary H I peaks outside the velocity range from $-25\,\mathrm{km\,s^{-1}}$ to $+12\,\mathrm{km\,s^{-1}}$.

[c] Abdo et al. (2011).

[d] While this object is not listed in the *IRAS* point source catalog, T_d is locally high around this object.

2. The two regions where there is a secondary H I peak outside the velocity range from $-25\,\mathrm{km\,s^{-1}}$ to $+12\,\mathrm{km\,s^{-1}}$ are masked at $(\ell, b) \sim (81.^\circ5, -33.^\circ0)$, $(85.^\circ6, -33.^\circ8)$. Generally, these secondary peaks show an intensity comparable to that of the main H I peak.
3. Regions with high T_d indicating localized heating by stars, etc., are masked by referring to the *IRAS* point source catalog, etc. The most extended region of such high T_d is located toward 3C 454.3, although the origin of the high T_d is not known.
4. The six regions where the H I data are missing are masked.

3. RESULTS

Figure 1 shows four panels that present CO, H I, and *Planck*/*IRAS* dust properties. Figure 1(a) shows the CO ($J = 1$–0) velocity integrated intensity distribution, W_CO ($\mathrm{K\,km\,s^{-1}}$). Figure 1(b) shows an overlay of H I and CO where we confirm the associated H I in previous works (Gir et al. 1994; Yamamoto et al. 2003). $W_\mathrm{H\,I}$ ($\mathrm{K\,km\,s^{-1}}$) is the intensity of H I integrated from $-49\,\mathrm{km\,s^{-1}}$ to $+17\,\mathrm{km\,s^{-1}}$. Figure 1(c) presents an overlay of τ_{353} and CO. The comparison shows good correspondence between them within the CO contours, whereas the correspondence of H I with τ_{353} seems less clear than in the case of CO. We note that τ_{353} is significantly extended beyond the lowest CO contour $3.4\,\mathrm{K\,km\,s^{-1}}$ (3σ). Figure 1(d) shows an overlay of T_d and CO. The lowest $T_\mathrm{d} \sim 16$ K is clearly associated with CO, and T_d increases up to ∼22 K outside the CO clouds.

Figure 2(a), where masking in Section 2.5 is applied, shows an average H I spectrum over the region in Figure 1, and Figure 2(b) shows the H I integrated intensity over the same longitude range where ^{12}CO ($J = 1$–0) intensity is superposed by black contours. Figure 2(a) indicates that most of the H I emission is in the range from $-25\,\mathrm{km\,s^{-1}}$ to $+12\,\mathrm{km\,s^{-1}}$, which is determined by the 10% level of the average H I spectrum, and the H I emission from $-25\,\mathrm{km\,s^{-1}}$ to $+12\,\mathrm{km\,s^{-1}}$ has a single component, which includes 89% of the H I integrated intensity. The remaining 11% of the H I emission is mainly on the negative velocity side at $V_\mathrm{LSR} < -25\,\mathrm{km\,s^{-1}}$. In order to eliminate possible contamination of the H I at $V_\mathrm{LSR} < -25\,\mathrm{km\,s^{-1}}$ we shall adopt the H I velocity range from $-25\,\mathrm{km\,s^{-1}}$ to $+12\,\mathrm{km\,s^{-1}}$ in the following analysis and call this the main H I cloud. This velocity range includes the H I which has been suggested to be associated with the CO clouds (Gir et al. 1994; Yamamoto et al. 2003) and more details are given in Appendix A on the H I velocity channel distributions (Figure 10).

In the following, τ_{353} and $W_\mathrm{H\,I}$ denote those quantities for the whole velocity range and τ_{353}(main) and $W_\mathrm{H\,I}$(main) for the main H I cloud only. The excluded velocity ranges from the main H I cloud have very weak H I intensity of $\lesssim 30\,\mathrm{K\,km\,s^{-1}}$ (Figure 2(b)) and it is likely that this H I is optically thin. $W_\mathrm{H\,I}$(main) is calculated from $W_\mathrm{H\,I}$ by subtracting the H I integrated intensity at $V_\mathrm{LSR} < -25\,\mathrm{km\,s^{-1}}$ and $V_\mathrm{LSR} > +12\,\mathrm{km\,s^{-1}}$. By adopting the relationship between τ_{353} and $W_\mathrm{H\,I}$ in the optically thin limit (see below), τ_{353}(main) is calculated from τ_{353} by subtracting a fraction of τ_{353} in proportion to $[W_\mathrm{H\,I} - W_\mathrm{H\,I}(\mathrm{main})]/W_\mathrm{H\,I}$, which corrects for the emission due to the velocity range excluded from H I main. The details of the subtraction are given in Appendix B.

Figures 3(a) and 4(a) show scatter plots between $W_\mathrm{H\,I}$ and τ_{353} for the main H I cloud and for the whole H I velocity span, respectively, in the region with masking (Section 2.5.). We note that Figures 3 and 4 show the same trend, as described below, indicating that the subtraction has a minor effect on the results as expected from the weakness of the subtracted H I intensity. The scattering is fairly large with correlation coefficients of ∼0.6 in both plots (Figures 3(a) and 4(a)). Since $W_\mathrm{H\,I}$ is supposed to be a good measure of the total H I in the optically thin approximation, τ_{353} should be highly correlated with $W_\mathrm{H\,I}$ if the H I is optically thin and if gas and dust are well mixed with uniform properties. The large scatter suggests that the dust properties may vary significantly and/or that the optically thin approximation for the H I gas may not be valid.

In Figures 3(b), (c), 4(b), and (c), we indicate T_d for every 0.5 K interval at each point in Figures 3(a) and 4(a). We made least-squares fits between $W_\mathrm{H\,I}$(main) and τ_{353}(main) by linear regression for each T_d range. Since the number of data points becomes less for the highest T_d, the fitting accuracy becomes worse for higher T_d. In particular, for $T_\mathrm{d} \geqslant 21.5$ K, the number of points becomes much less than for the others; here we assume that the intercept is zero and determine only the slope. The slopes k ($\mathrm{K\,km\,s^{-1}}$), intercepts, and correlation coefficients are listed in Table 2. We note that the correlation coefficient is around 0.7–0.9 for T_d higher than 18 K. This clearly shows that the correlation strongly depends on T_d and becomes better for smaller T_d ranges; generally speaking, the slope becomes steeper and the intercept smaller with increasing T_d.

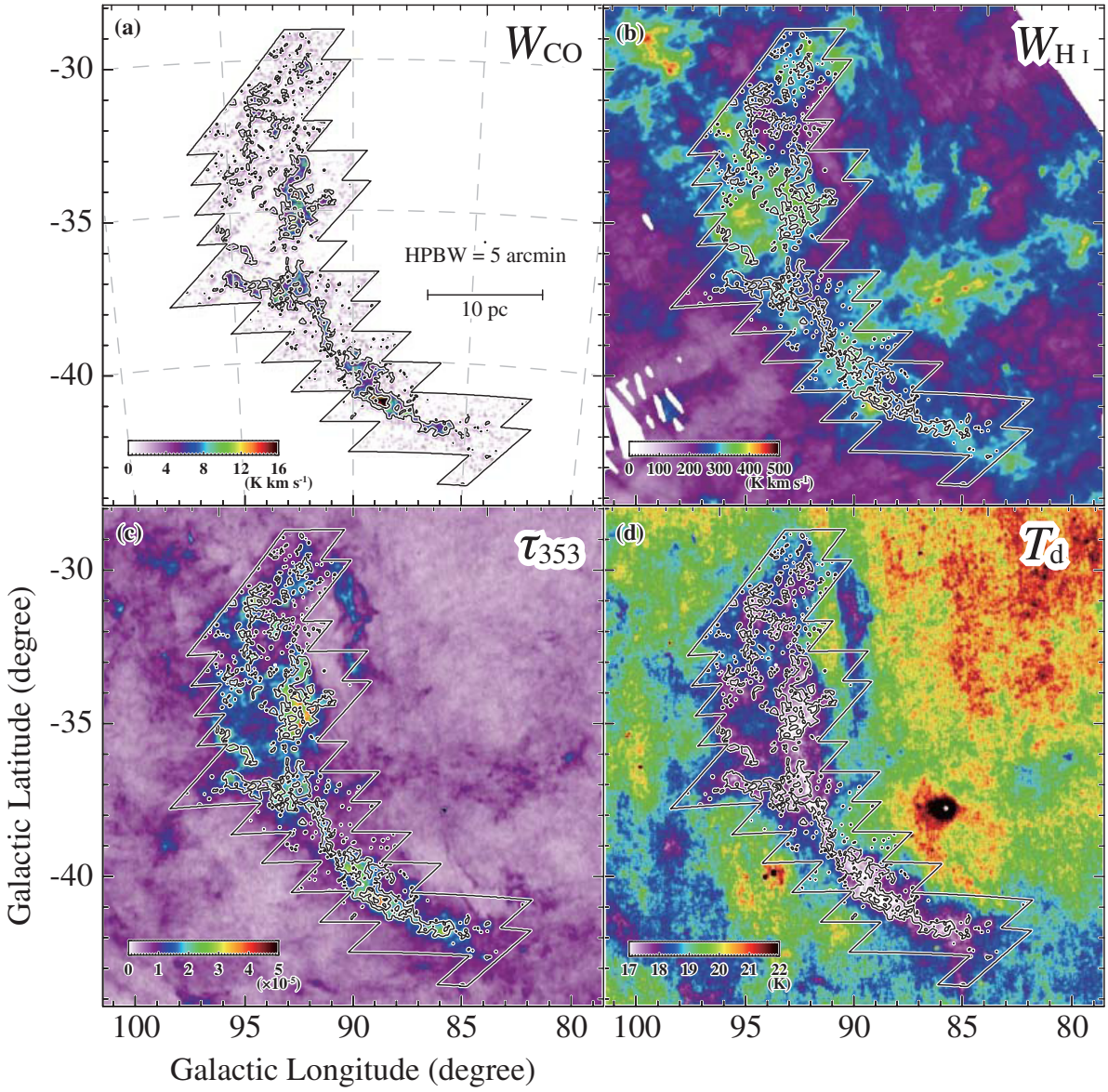

Figure 1. (a) Velocity-integrated intensity map of ^{12}CO(J = 1–0) in the galactic coordinates. The integrated LSR-velocity range is from −12 km s^{-1} to +2 km s^{-1}. The contours are drawn every 7.9 K km s^{-1} from 3.4 K km s^{-1}. The bounding box shows the observed area. (b)–(d) are spatial distributions of the velocity-integrated intensity of the H I ($W_{H\,I}$), the optical depth at 353 GHz (τ_{353}), and the temperature of the cold dust (T_d), respectively. The contours of CO and the bounding boxes are the same as in (a). The integrated velocity range of the $W_{H\,I}$ in (b) is from −49 km s^{-1} to +17 km s^{-1}. The effective beam sizes are 5 arcmin for the four panels.

(A color version of this figure is available in the online journal.)

Figure 5(a) shows a scatter plot of T_d and τ_{353}(main) and clearly indicates a significant decrease of T_d with τ_{353}(main). A similar result where the dust temperature increases with decreasing gas column density was recently found by the *Planck* Collaboration (*Planck* Collaboration et al. 2014a, 2014b). Figure 5(b) shows a scatter plot of W_{CO} and τ_{353}(main) in the area observed in CO. This shows a positive correlation with a correlation coefficient of ∼0.7, while the dispersion is large. The solid line in (b) represents a relationship τ_{353}(main) = $[(1.8 \pm 0.8) \times 10^{-6}] \cdot W_{CO}$ (K km s^{-1}) + $[(8.4 \pm 5.0) \times 10^{-6}]$, which is the result of a least-squares fit to the data with $W_{CO} \geqslant 3\sigma$.

4. ANALYSIS

From the behavior in Figure 3, we infer that for the highest T_d, the optically thin approximation of H I is valid, whereas for lower T_d, the approximation becomes worse due to the large H I optical depth. Equation (1) is used to estimate $N_{H\,I}$ for the optically thin part in Figure 3,

$$N_{H\,I}\,(\mathrm{cm}^{-2}) = (1.823 \times 10^{18}) \cdot W_{H\,I}\,(\mathrm{K\,km\,s}^{-1}), \qquad (1)$$

and the relationship between τ_{353}(main) and $N_{H\,I}$(main) is estimated for the optically thin regime at $T_d \geqslant 21.5$ K;

$$N_{H\,I}(\mathrm{main})\,(\mathrm{cm}^{-2}) = (1.5 \times 10^{26}) \cdot \tau_{353}(\mathrm{main}), \qquad (2)$$

where 1.5×10^{26} is calculated by a product of 1.823×10^{18} in Equation (1) and the slope k (= 8.47×10^{7} K km s^{-1}) for $T_d > 21.5$ K in Table 2.

Relation (2) holds as long as the dust properties are uniform, allowing us to calculate $N_{H\,I}$(main) from τ_{353}(main). Then the coupled Equations (3) and (4) in the following are used to

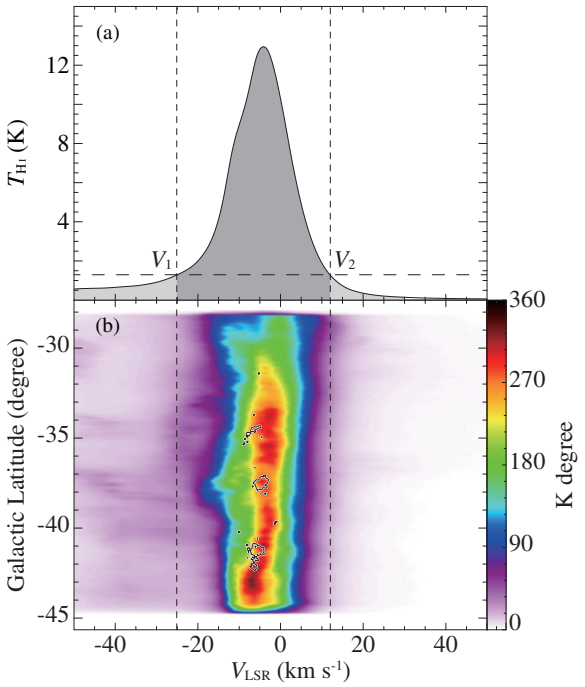

Figure 2. (a) Average spectrum of the H I in the region shown in Figure 1(d), but with the masking described in Section 2.5 applied. $T_{\rm mb}$ at $V_1 = -25\,{\rm km\,s^{-1}}$ and at $V_2 = +12\,{\rm km\,s^{-1}}$ correspond to the 10% level of the peak. (b) Latitude-velocity diagram of H I (color image) and CO (contours) integrated over the longitude range in Figure 1. The integrating range is from $\ell \sim 80°$ to $\sim 100°$. The level of the CO contours is ~ 3 K deg. 89% of the H I emission is concentrated in the velocity range $-25\,{\rm km\,s^{-1}}$ to $+12\,{\rm km\,s^{-1}}$.

(A color version of this figure is available in the online journal.)

solve for $T_{\rm s}$ and $\tau_{\rm H\,I}$(main), where $N_{\rm H\,I}$(main) is calculated from τ_{353}(main) by Equation (2),

$$W_{\rm H\,I}({\rm main})\,({\rm K\,km\,s^{-1}}) = [T_{\rm s}\,({\rm K}) - T_{\rm bg}\,({\rm K})] \cdot \Delta V_{\rm H\,I}\,({\rm km\,s^{-1}}) \cdot [1 - \exp(-\tau_{\rm H\,I}({\rm main}))], \quad (3)$$

$$\tau_{\rm H\,I}({\rm main}) = \frac{N_{\rm H\,I}({\rm main})\,({\rm cm^{-2}})}{1.823 \times 10^{18}} \cdot \frac{1}{T_{\rm s}\,({\rm K})} \cdot \frac{1}{\Delta V_{\rm H\,I}\,({\rm km\,s^{-1}})}, \quad (4)$$

where $\Delta V_{\rm H\,I}$, the H I linewidth, is given by $W_{\rm H\,I}$(main)/(peak H I brightness temperature) and $T_{\rm bg}$ is the background continuum radiation temperature (see Section 2.4.) including the 2.7 K cosmic background radiation (Fixsen 2009). $\tau_{\rm H\,I}$(main) is the H I optical depth averaged over the H I velocity width $\Delta V_{\rm H\,I}$, which ranges from $8\,{\rm km\,s^{-1}}$ to $30\,{\rm km\,s^{-1}}$ with a median at $\sim 14\,{\rm km\,s^{-1}}$. Note that Equation (4) is valid not only for small $\tau_{\rm H\,I}$ but also for any positive value of $\tau_{\rm H\,I}$. Figure 6 shows the two relationships in the $T_{\rm s}$–$\tau_{\rm H\,I}$(main) plane for four typical values of $T_{\rm s} \simeq 20$ K (a), 40 K (b), 60 K (c), and 80 K (d). We estimate the errors in $T_{\rm s}$ as shown in Figure 6 from the 1σ noise level of the H I and τ_{353}(main) data. We find that the equations give reasonable solutions with small errors for lower $T_{\rm s}$, whereas they cannot give a single set of $T_{\rm s}$ and $\tau_{\rm H\,I}$(main) for $T_{\rm s}$ higher than ~ 70 K, where the error bars in $T_{\rm s}$ become uncomfortably large. In Figure 6, we estimate the error ranges as follows: (a) $T_{\rm s} \simeq 20^{+4}_{-2}$ K, $\tau_{\rm H\,I}$(main) $\simeq 1.06^{+0.28}_{-0.29}$, (b) $T_{\rm s} \simeq 40^{+13}_{-6}$ K, $\tau_{\rm H\,I}$(main) $\simeq 0.84^{+0.28}_{-0.29}$, (c) $T_{\rm s} \simeq 60^{+126}_{-20}$ K, $\tau_{\rm H\,I}$(main) $\simeq 0.31^{+0.21}_{-0.22}$, and (d) $T_{\rm s} \simeq 80^{+\infty}_{-39}$ K, $\tau_{\rm H\,I}$(main) $\simeq 0.16^{+0.20}_{-0.16}$. In the optically thin limit, the two equations become

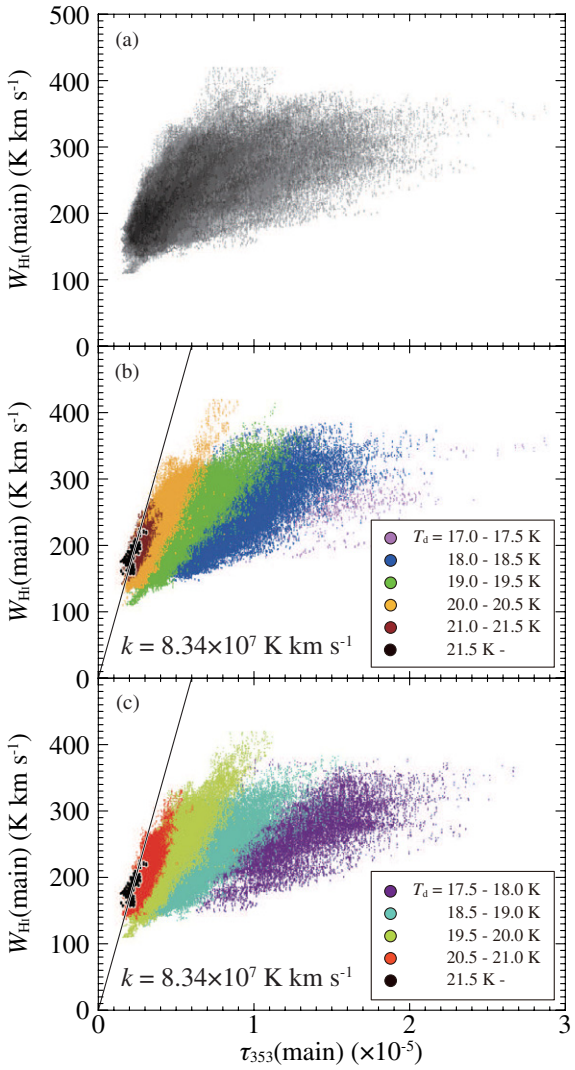

Figure 3. Scatter plots between $W_{\rm H\,I}$(main) and τ_{353}(main) and between $W_{\rm H\,I}$ and τ_{353} in the region shown in Figure 1. Specific areas are masked. Details on the masking are described in Section 2.5. Scatter plots of $W_{\rm H\,I}$(main) whose integrated velocity range is from $-25\,{\rm km\,s^{-1}}$ to $+12\,{\rm km\,s^{-1}}$ and τ_{353}(main), which is the τ_{353} component associated with the H I whose velocity range is from $-25\,{\rm km\,s^{-1}}$ to $+12\,{\rm km\,s^{-1}}$. Details on how to calculate this τ_{353}(main) value are described in Appendix B. (a) plots in black dots for all points. (b) and (c) show the scatter plots for $T_{\rm d}$ in windows of 0.5 K intervals every 1 K. In order to avoid heavy overlapping among the data points, in (b) we show five $T_{\rm d}$ ranges, 17.0–17.5 K (light purple), 18.0–18.5 K (blue), 19.0–19.5 K (green), 20.0–20.5 K (yellow), and 21.0–21.5 K (brown), and in (c) five $T_{\rm d}$ ranges shifted by 0.5 K, 17.5–18.0 K (purple), 18.5–19.0 K (light blue), 19.5–20.0 K (light green), and 20.5–21.0 K (red). In both panels (b) and (c), the $T_{\rm d}$ range, 21.5 K and higher, is shown in black along with the linear regression line obtained by the least-squares fit which is assumed to have zero intercept.

(A color version of this figure is available in the online journal.)

essentially the same, and can be satisfied by an infinite number of solutions, either a combination of large $T_{\rm s}$ and small $\tau_{\rm H\,I}$(main) or of small $T_{\rm s}$ and large $\tau_{\rm H\,I}$(main). Only the lower limit for $T_{\rm s}$ and the upper limit of $\tau_{\rm H\,I}$(main) are constrained.

Figure 7(a) shows the distribution of $T_{\rm s}$, Figure 7(b) the distribution for $\tau_{\rm H\,I}$(main), and Figure 7(c) the distribution of τ_{353}(main). Several specific areas are masked as described in Section 3 and also masked where the estimated $T_{\rm s}$ is greater than 70 K. In Figure 7(a) $T_{\rm s}$ is mostly lower than 50 K. We also find that $\tau_{\rm H\,I}$(main) becomes large in many of the data points. The results for estimated $T_{\rm s}$ and $\tau_{\rm H\,I}$(main) are plotted in Figure 8 with a superposition of Equation (3) for $T_{\rm s}$ from 10 K to

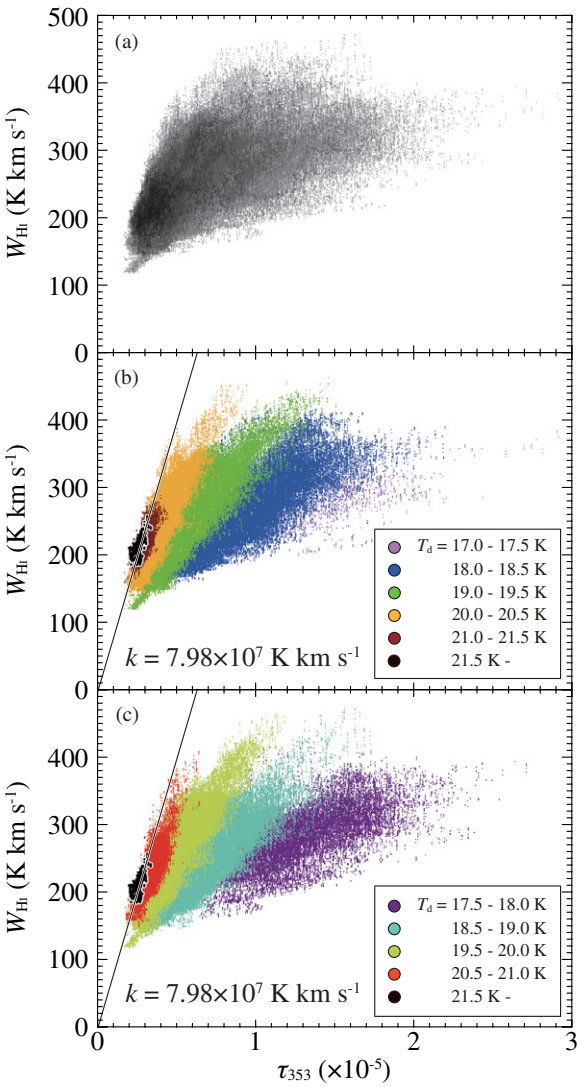

Figure 4. Same as Figure 3 but integrated velocity range of the H I is from −49 km s^{-1} to +17 km s^{-1} and τ_{353} is the total value.

(A color version of this figure is available in the online journal.)

Table 2
Parameters of the Data Points in Each T_d Range

T_d (K)	N_{pixel}	Slope k (K km s^{-1})	Intercept (K km s^{-1})	C.C.
17.0–17.5	1.48 × 10^3	6.83 × 10^6	1.5 × 10^2	0.62
17.5–18.0	2.73 × 10^4	9.85 × 10^6	1.4 × 10^2	0.72
18.0–18.5	8.64 × 10^4	1.41 × 10^7	1.2 × 10^2	0.80
18.5–19.0	1.53 × 10^5	1.92 × 10^7	1.1 × 10^2	0.81
19.0–19.5	1.61 × 10^5	2.50 × 10^7	0.96 × 10^2	0.86
19.5–20.0	1.42 × 10^5	3.24 × 10^7	0.88 × 10^2	0.88
20.0–20.5	9.52 × 10^4	4.03 × 10^7	0.77 × 10^2	0.86
20.5–21.0	4.33 × 10^4	4.08 × 10^7	0.81 × 10^2	0.79
21.0–21.5	1.13 × 10^4	3.54 × 10^7	1.0 × 10^2	0.71
⩾21.5	7.18 × 10^2	8.34 × 10^7	···	0.62

Notes. N_{pixel} is the number of pixels in each T_d range. C.C. indicates the correlation coefficients for the points in each T_d range. Columns 3 and 4 give values of the slope and intercept of the best fit linear relationship between W_{HI}(main) and τ_{353}(main) (Figure 3). The last row gives the slope assuming the intercept is zero in this case. The data are fitted by least-squares method.

100 K with τ_{HI}(main). We see saturation of W_{HI}(main) becomes important for lower T_s, and the slope for a given T_s decreases

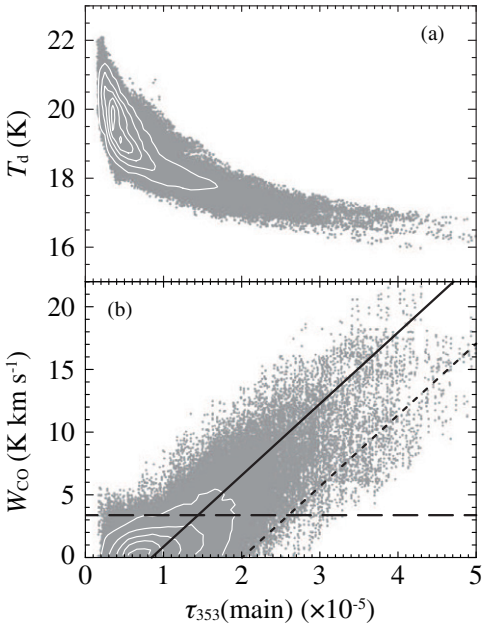

Figure 5. (a) Correlation plot between T_d and τ_{353}(main) in the area shown in Figure 7(c). The contours represent the 90%, 70%, 50%, 30%, and 10% levels of the maximum of the density of the plotted data over the (T_d, τ_{353}(main)) space. (b) same as (a) but for W_{CO} and τ_{353}(main). The contours represent the 90%, 70%, 50%, 30%, and 10% levels of the maximum of the density of the plotted data over the (W_{CO}, τ_{353}(main)) space. The dashed line represents 3σ level of the CO data (3.4 K km s^{-1}) and the solid line represents a relationship $\tau_{353}(\text{main}) = [(1.8 \pm 0.8) \times 10^{-6}] \cdot W_{CO}\,(\text{K km s}^{-1}) + [(8.4 \pm 5.0) \times 10^{-6}]$, which is the result of a least-squares fit to the data with $W_{CO} > 3\sigma$. The dotted line is $\tau_{353}(\text{main}) = (1.8 \times 10^{-6}) \cdot W_{CO}\,(\text{K km s}^{-1}) + (2 \times 10^{-5})$ (see text).

with decreasing T_s due to saturation. This result is consistent with T_s estimated from comparisons between H I emission and absorption toward radio continuum sources, which show that cold H I clouds of 20–40 K are common (Dickey et al. 2003; Heiles & Troland 2003). Their spatial coverage is, however, much smaller than the present coverage, 100 deg^2. Possible hints of optically thick H I are also found in the literature (Strasser & Taylor 2004; Dickey 2010).

5. PHYSICAL CONDITIONS IN THE H I GAS

5.1. T_d and T_s

The present analysis offers evidence for a significant fraction of cold H I gas in the region. The analysis shows typical physical parameters for the optically thick H I gas as follows: N_{HI}(main) = 4 × 10^{20}–1.5 × 10^{21} cm^{-2}, H I number density n_{HI} = 40–160 cm^{-3} for a cloud line-of-sight depth of 3 pc, and T_s =20–40 K. The gas kinetic temperature of the H I is determined by heating due to the ISRF and cooling mainly by the C II line (e.g., Wolfire et al. 1995) and is in a range of 10–100 K for a column density higher than 2 × 10^{20} cm^{-2} (e.g., Goldsmith et al. 2007). Since the radiative transition rate, the Einstein A coefficient, of the 21 cm line is small, ∼3 × 10^{-15} s^{-1}, the 21 cm transition is well thermalized by collisional excitation for a density higher than ∼10 cm^{-3} (e.g., Liszt 2001; Sato & Fukui 1978). T_s is exactly in equilibrium with the gas kinetic temperature in the dense H I gas. On the other hand, T_d is determined by the balance between the ISRF heating and thermal radiation of dust grains and is generally in a range from 15 K to 25 K in the H I gas. T_d and T_s should show a correlation since heating is commonly due to the ISRF, where T_d variation is much smaller than that of T_s due to the strong temperature

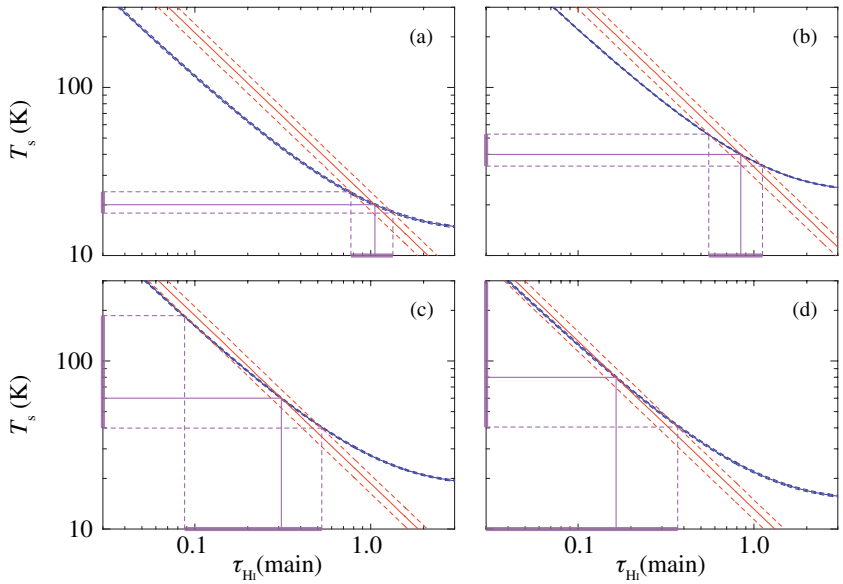

Figure 6. Blue and red lines represent Equations (3) and (4) in the text, respectively. The crossing point of the two lines is the solution that satisfies both Equations (3) and (4). (a), (b), (c), and (d) show typical cases of the solutions of $T_s \simeq 20$ K, $\simeq$40 K, $\simeq$60 K, and $\simeq$80 K, and are located at $(\ell, b) \sim (92.^\circ70, -41.^\circ56)$, $(90.^\circ07, -42.^\circ68)$, $(89.^\circ69, -29.^\circ12)$, and $(86.^\circ03, -30.^\circ09)$, respectively. The dashed lines around each line are the error taking observational parameters into consideration. The purple solid lines indicate the solutions of $\tau_{\rm H\,I}$(main) and T_s and dashed lines show their errors.

(A color version of this figure is available in the online journal.)

dependence of the dust cooling, as $(T_d)^6$ (e.g., Draine 2011). For A_V more than 1 mag, T_s becomes less than 60 K (e.g., Goldsmith et al. 2007) and T_d shows a significant decrease to 17 K, which corresponds to T_d within the CO clouds (Figure 1). The present results on T_s and $\tau_{\rm H\,I}$(main) are therefore consistent with the thermal properties of the ISM. It is possible that T_d is affected by the local radiation field in addition to the general ISRF. The distribution of T_d shown in Figure 1(d) indicates that in the northwest of the CO clouds T_d tends to be higher than in the southeast. This may be due to the excess radiation field of the OB stars in the Sco OB2 association which are located 100–200 pc away from the present clouds (see Tachihara et al. 2001).

An $X_{\rm CO}$ factor converting $W_{\rm CO}$ into $N_{\rm H_2}$ is estimated from a comparison of CO and τ_{353}(main) (Figure 5(b)). A least-squares fit for $W_{\rm CO}$ greater than 3.4 K km s^{-1} (above the 3σ noise level) yields τ_{353}(main) $= [(1.8 \pm 0.8) \times 10^{-6}] \cdot W_{\rm CO}$ (K km s^{-1}) + $[(8.4 \pm 5.0) \times 10^{-6}]$. Here we adopt $W_{\rm CO}$ greater than 3σ by considering that an $X_{\rm CO}$ factor is conventionally estimated for $A_V \gtrsim$ 2–3 mag (e.g., Bell et al. 2006). The offset of 8.4×10^{-6} in τ_{353}(main) in the above relationship is interpolated as due to the contribution of the H I, and the $X_{\rm CO}$ factor is calculated from the slope 1.8×10^{-6} in the relationship and the coefficient in Equation (2) as $X_{\rm CO} = N_{\rm H_2}/W_{\rm CO} = (1.5 \times 10^{26}/2) \times (1.8 \times 10^{-6}) = 1.3 \times 10^{20}$ cm^{-2} (K km s^{-1}) with a typical dispersion of $\sim \pm$40%, which is somewhat smaller than that estimated elsewhere, (2–3) $\times 10^{20}$ cm^{-2} (K km s^{-1}) (e.g., Bertsch et al. 1993). Numerical simulations suggest that the $X_{\rm CO}$ factor is relatively uniform in regions of high visual extinction where CO is intense (Inoue & Inutsuka 2012; Glover & Mac Low 2011; Bell et al. 2006). This difference may be possibly ascribed to the large contribution of cold H I gas which was not taken into account previously and should be confirmed by a careful analysis of more sample clouds. We note that we see a small number of points in Figure 5(b) which show higher τ_{353}(main) for a given $W_{\rm CO}$ on the right of the dotted line and above the dashed line. These may correspond to molecular gas with slightly less CO abundance than the majority, suggesting a younger chemical evolutionary stage (Yamamoto et al. 2003) and can be characterized by a higher $X_{\rm CO}$ factor.

5.2. Alternative Ideas

The above interpretation assumes that all the neutral gas outside the CO is purely atomic. This interpretation is consistent with the present analysis including only H I as shown by the fit of the line radiation transfer equation and estimated T_s and $\tau_{\rm H\,I}$(main) (Figure 7). We shall test if an interpretation based on CO-free H_2 is possible as an alternative, which was advocated for a giant molecular cloud having a total mass of 10^5–10^6 $M_\odot$ by Wolfire et al. (2010) and was discussed in the first *Planck* paper (*Planck* Collaboration et al. 2011b). τ_{353}(main) is a sum of the dust opacity in both the H I and H_2 gas. If CO-free H_2 is dominant, H_2 may account for most of the τ_{353}(main) instead of H I. The observed value of $W_{\rm H\,I}$(main) poses a strict lower limit on $N_{\rm H\,I}$(main) and it is not probable that H_2 dominates H I. The majority of the data points have $T_s \sim 30$ K (Figure 8) and a lower limit for their H I column density is given by the optically thin limit. For instance, for points having $W_{\rm H\,I}$(main) = 250 K km s^{-1}, $N_{\rm H\,I}$(main) at $T_s \sim 30$ K is 0.85×10^{21} cm^{-2}, whereas $N_{\rm H\,I}$(main) in the optically thin limit is 0.45×10^{21} cm^{-2} corresponding to $\sim$50% of 0.85×10^{21} cm^{-2}, and for points having $W_{\rm H\,I}$(main) = 200 K km s^{-1}, $N_{\rm H\,I}$(main) at $T_s \sim 30$ K is 0.6×10^{21} cm^{-2} whereas $N_{\rm H\,I}$(main) in the optically thin limit is 0.35×10^{21} cm^{-2} corresponding to $\sim$60% of 0.6×10^{21} cm^{-2}. This suggests that the cold gas typically has an H_2 abundance of 50% or less over most of the region outside of the CO clouds. Direct UV absorption measurements of H_2 abundances on the line of sight toward NGC 7469 ($\ell = 83.^\circ10$, $b = -45.^\circ47$) show $N_{\rm H_2} = 4.7 \times 10^{19}$ cm^{-2} and $N_{\rm H\,I} = 3.9 \times 10^{20}$ cm^{-2} (Gillmon et al. 2006), indicating that the hydrogen is about 90% atomic. It is worth noting that other lines of sight at intermediate latitudes observed by *FUSE* and *Copernicus* (summarized by Rachford et al. 2009) show similarly low molecular fractions unless the total H column density, $N_{\rm H_2} + N_{\rm H\,I} \gtrsim 10^{21}$ cm^{-2}, lending support for the conclusion that H I is dominant. Finally, we note that the

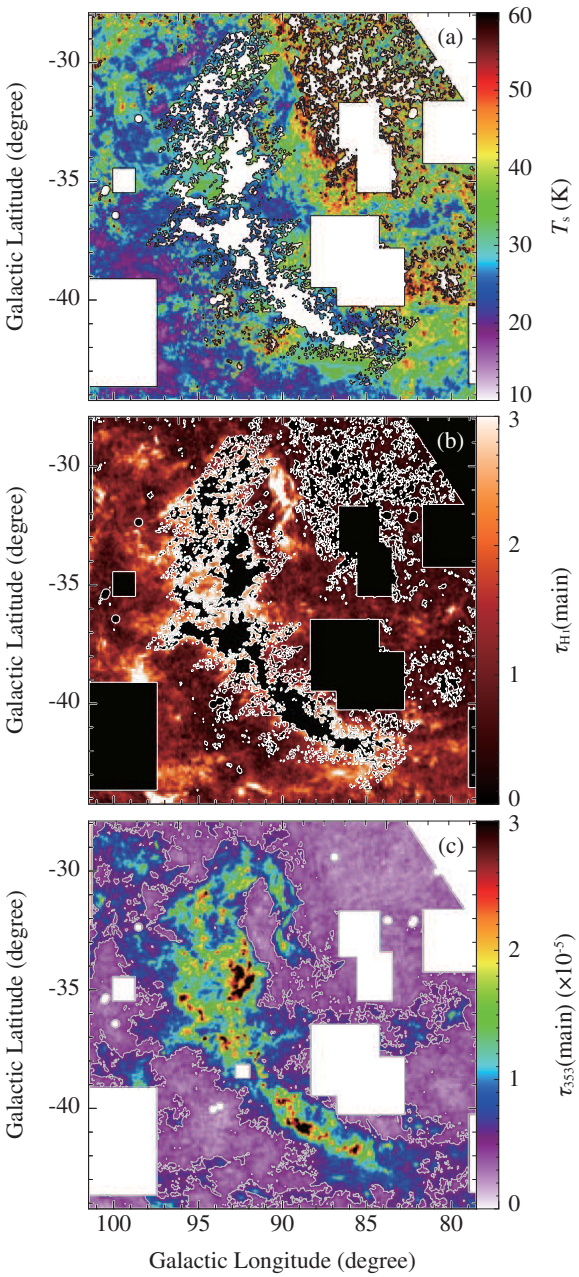

Figure 7. Panels (a) and (b) show the spatial distribution of T_s and τ_{H1}(main) solved from the two Equations (3) and (4) in the text. The masks described in Section 2.5 are applied and in addition, the areas where $T_s \geqslant 70$ K are masked. (c) represents the spatial distribution of τ_{353}(main). The gray contours indicate the level of τ_{353}(main) $= 5 \times 10^{-6}$.

(A color version of this figure is available in the online journal.)

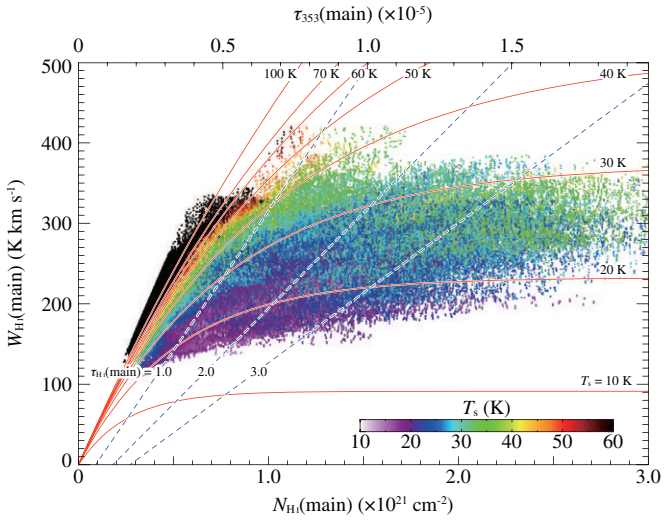

Figure 8. Correlation plot between W_{H1}(main) and N_{H1}(main). The data in the region shown in Figures 7(a) and (b) are plotted. The color of each point represents T_s. The solid and dashed lines represent T_s and τ_{H1}(main) calculated from Equations (3) and (4) in the text by assuming ΔV_{H1} of ∼14.1 km s^{-1} (median value) and T_{bg} of ∼3.5 K (median value), respectively.

(A color version of this figure is available in the online journal.)

timescale for H_2 formation is generally as long as 10^7 yr for a typical density of 100 cm^{-3} (Hollenbach et al. 1971). The cloud lifetime is, however, smaller than $\sim 10^6$ yr as estimated from the crossing time at latitudes higher than 10° for a typical cloud size of several parsecs and a line width of 15 km s^{-1} (Yamamoto et al. 2003, 2006). This suggests that the present cloud is too young to form significant H_2. Another possibility is that the dust properties may be considerably different in the region, as has been explored by the *Planck* collaboration (*Planck* Collaboration et al. 2014a). We shall defer exploration of this possibility until a full account of the study is opened to the community.

5.3. Mass of the H I Envelope

We estimate the total mass of the clouds in the region under study. We estimate the total system mass including H I, H_2, and He (40% of hydrogen in mass) to be $\sim 1.3 \times 10^4\ M_\odot$, by using the sum of τ_{353}(main) above 5×10^{-6} under Equation (2) applied to both H I and H_2 (Figure 7(c)). The typical ratio of the opacity-corrected case to the optically thin case is estimated to be ∼2.7 toward areas without CO emission, showing that the opacity correction has a significant impact. The mass of the H I gas in the masked areas is interpolated to be $\sim 9.0 \times 10^2\ M_\odot$ by using the average N_{H1}(main) $\sim 1.3 \times 10^{21}$ cm^{-2} in the areas without masking and corresponds to ∼7% of the total system mass above. On the other hand, the molecular mass is estimated to be $\sim 1.2 \times 10^3\ M_\odot$ by applying the present X_{CO} factor ($=1.3 \times 10^{20}$ cm^{-2} (K km s^{-1})$^{-1}$) to the CO emission. Here we integrated the CO emission above the 3σ noise fluctuations of 3.4 K km s^{-1} in the integrated intensity in the 5 arcmin smoothed beam. By subtracting this mass from the total system mass, we obtain $\sim 1.2 \times 10^4\ M_\odot$ as the total mass of the H I envelope. We thus find that the H I envelope has a total mass ∼10 times larger than the mass of the H_2 clouds probed by CO. Note that in Gir et al. (1994) the mass of the H I envelope was calculated as $\sim 3 \times 10^3\ M_\odot$, which is smaller than the present result. This difference may be attributed to the fact that (1) the area they used for the calculation corresponds to ∼1/2 of that used in our calculation, and (2) they assumed that all the H I gas is optically thin.

We conclude that the H_2 clouds traced by CO are surrounded by massive, optically thick H I envelopes possibly containing a relatively small fraction of H_2 that has no corresponding CO emission above the 3σ noise fluctuations of 3.4 K km s^{-1}. Figure 9 is a histogram of the mass of the H I envelope as a function of T_s. This clearly shows that most of the H I is in the T_s range of 20–40 K. Assuming the depth of the H I envelope along the line of sight to be 3 pc, the H I density is estimated to be 40–160 cm^{-3}. This density is consistent with $T_s = 20$–40 K in a model calculation of the thermal balance (Goldsmith et al. 2007).

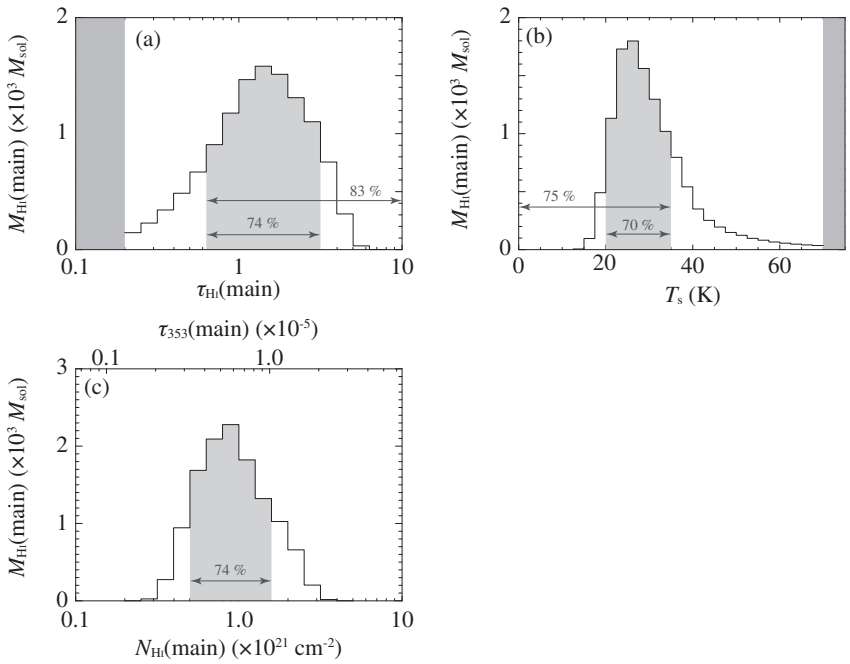

Figure 9. (a) Histogram of the mass of the H I envelope as a function of τ_{H1}(main). (b) The same as (a), but as a function of T_s. (c) The same as (a) and (b), but as functions of N_{H1}(main) and τ_{353}(main). The areas filled with light gray are determined by the widths at the half-levels of each histogram. Note that in panels (a) and (b), the histograms where τ_{H1}(main) $\leqslant 0.2$ or $T_s \geqslant 70$ K are masked because the solutions of τ_{H1}(main) and T_s are not well-estimated.

It is generally known that small clouds having a mass less than $\sim$1000 $M_\odot$ cannot be gravitationally bound due to the large virial mass as compared with the CO luminosity mass (e.g., Yonekura et al. 1997; Kawamura et al. 1998). The H I envelope may have a deep influence on cloud dynamics. The average density of the H I is 100 cm^{-3} and the velocity width is 15 km s^{-1}. The dynamical pressure of H I, $\rho\, v^2$ ((density) · (velocity dispersion)^2) is nearly equal to that of the H_2 gas and the pressure exerted by the H I envelope is able to confine the H_2. The H I envelope may help to stabilize small H_2 clouds yet it is perhaps true that the whole system, including the H I envelope, is not gravitationally bound because of the large velocity dispersion of the H I and some dynamically transient states, like those in colliding H I flows, must be invoked to explain the cloud dynamics (e.g., Hartmann et al. 2001).

5.4. Relation to the Dark Gas

Recent analyses of gamma-ray maps and the *Planck* data show evidence for dark gas which is not seen in CO or H I emission (Grenier et al. 2005; *Planck* Collaboration et al. 2011b). These analyses did not consider the H I opacity effect and assumed that H I is completely optically thin. The present study has shown that the H I optical depth effect is important in this region and an upward correction of the cloud mass by a factor of $\sim$2 on average is required. A significant fraction of the relatively dense H I gas may therefore be masked by saturation of the 21 cm line, and the cold H I gas is a viable candidate for the dark gas. This possibility deserves further exploration by including a much larger fraction of the sky. We note that the present analysis is applicable in a τ_{353}(main) range of 2×10^{-6} to a few $\times\, 10^{-5}$. Therefore, the behavior of the H I outside this range has yet to be explored separately.

6. CONCLUSIONS

We have made a comparison of H I, CO, and the *Planck* dust properties in a complex of high latitude clouds MBM 53, 54, 55 and HLCG 92−35. Our conclusions from this study are as follows.

The H I intensity shows a poor correlation with dust opacity with a correlation coefficient of $\sim$0.6. We interpret that this is caused by the effect of the optical depth on 21 cm H I emission. We present a method for estimating the spin temperature and the optical depth of the H I emission which couples the equation of line radiation transfer and the expression for the H I optical depth by assuming that dust properties do not change significantly in the region, where the τ_{353}(main) is limited to the range 3×10^{-6} to 2×10^{-5}. We have analyzed about 8×10^5 data points smoothed at 5 arcmin resolution and successfully estimated T_s and τ_{H1}(main). Most of the points have T_s in the range from 20 K to 40 K and τ_{H1}(main) is in the range from 0.2 to 4. This indicates that saturation due to a large H I optical depth provides a reasonable explanation of the suppressed H I intensity in regions with large dust opacity. The T_s distribution is consistent with previous results estimated from absorption measurements toward radio continuum sources while in this paper, the spatial coverage is continuous, covering a much larger area than continuum source absorption measurements. If the present results are correct, this suggests that optically thick H I is more significant than previously assumed in the literature. The typical physical parameters of the cold H I are density 40–160 cm^{-3} T_s = 20–40 K and N_{H1}(main) = 4×10^{20}–1.5×10^{21} cm^{-2}. The X_{CO} factor to convert W_{CO} into N_{H_2} has been estimated to be 1.3×10^{20} cm^{-2} (K km s^{-1}). The CO clouds are associated with a massive dense cold H I envelope having $\sim 1.2 \times 10^4$ $M_\odot$ compared with the CO cloud mass of $\sim 1.2 \times 10^3$ $M_\odot$. Another possibility, that the dust properties may vary significantly, is being explored currently by the *Planck* collaboration and should be considered in depth as a future step. Finally, it is an obvious

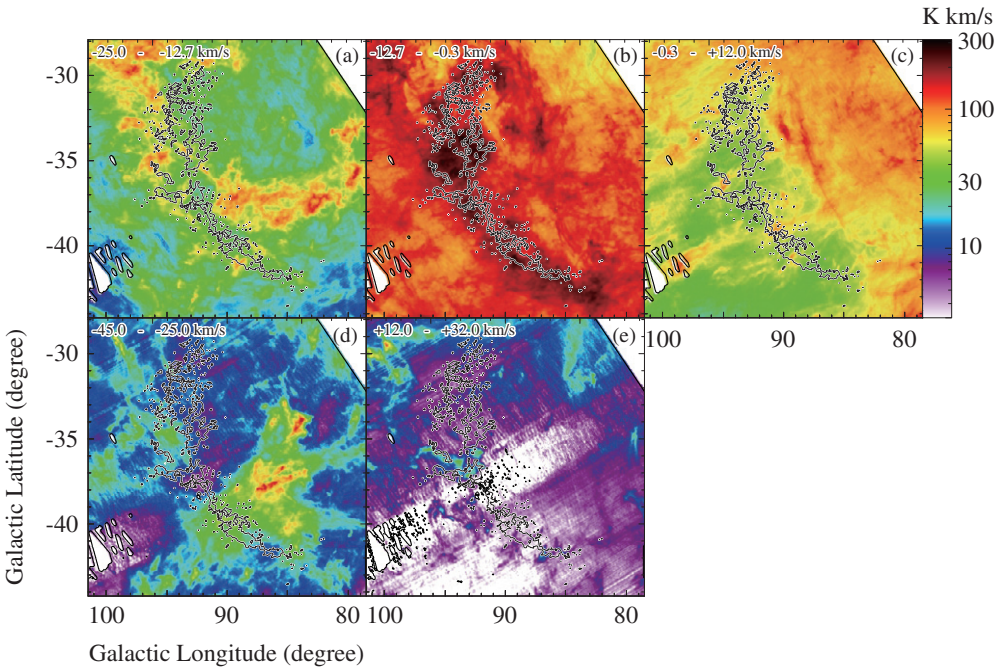

Figure 10. Velocity channel maps of the H I (color image) superposed on the W_{CO} (contours). In panels (a)–(c), we show the channel maps of the main H I cloud dividing the velocity range into three. Panels (d) and (e) show the channel maps outside the main H I velocity range. The contour level of W_{CO} is 3.4 K km s^{-1} for each panel.

(A color version of this figure is available in the online journal.)

task to extend this method to the whole sky to see if cold H I is common and dominant in the local interstellar space around the Sun.

We are grateful to François Boulanger and Jean-Phillippe Bernard for their initiative to begin the collaboration between *Planck* and NANTEN2. The high latitude clouds in the paper were chosen as one of the primary targets in the comparative study. We thank the anonymous referee for valuable comments on the paper.

NANTEN2 is an international collaboration among 10 universities: Nagoya University, Osaka Prefecture University, University of Cologne, University of Bonn, Seoul National University, University of Chile, University of New South Wales, Macquarie University, University of Sydney, and University of ETH Zurich. This work was financially supported by Grants-in-Aid for Scientific Research (KAKENHI) of the Japanese society for the Promotion of Science (JSPS; grant numbers 24224005, 25287035, 23403001, 23540277, and 23740149-01). This work was also financially supported by the Young Research Overseas Visits Program for Vitalizing Brain Circulation (R2211) and the Institutional Program for Young Researcher Overseas Visits (R29) by the JSPS and by the grant-in-aid for Nagoya University Global COE Program, "Quest for Fundamental Principles in the Universe: From Particles to the Solar System and the Cosmos," from MEXT. Based on observations obtained with *Planck* (http://www.esa.int/Planck), an ESA science mission with instruments and contributions directly funded by ESA Member States, NASA, and Canada. This publication utilizes data from Galactic ALFA H I (GALFA H I) survey data set obtained with the Arecibo *L*-band Feed Array (ALFA) on the Arecibo 305 m telescope. Arecibo Observatory is part of the National Astronomy and Ionosphere Center, which is operated by Cornell University under Cooperative Agreement with the U.S. National Science Foundation. The GALFA H I surveys are funded by the NSF through grants to Columbia University, the University of Wisconsin, and the University of California. Some of the results in this paper have been estimated using the HEALPIX (Górski et al. 2005) package.

APPENDIX A

Figure 10 shows five H I velocity channel distributions from $V_{LSR} = -45$ km s^{-1} to +32 km s^{-1}. The main H I cloud toward the CO emitting clouds is seen from -12.7 km s^{-1} to -0.3 km s^{-1} (panel (b)) as noted by Gir et al. (1994). The main feature is outstanding in the H I intensity having 200 K km s^{-1} in the integrated intensity. In this velocity channel, we see additional H I features; one is located ∼5° west of the main cloud and is elongated in a similar direction and with a similar length to the main cloud (called West1 H I), and the other is in the north of the main cloud peaked at $(l, b) \sim (100°, -31°)$ (North H I). West1 H I seems to be linked with the northern tip of the CO clouds. We also find an additional feature (West2 H I) peaked at $(l, b) \sim (90°, -37°)$ which may be extended to the west up to $l \sim 80°$.

In V_{LSR} from -25.0 km s^{-1} to -12.7 km s^{-1} (panel (a)), we see two features; one of them corresponds to North H I in position and the other to West2 H I. In addition, the H I, North H I, and several smaller peaks along the southern rim of the main cloud, seem to be surrounding the CO, as noted by Yamamoto et al. (2003, see also their Figure 6).

In the velocity from -0.3 km s^{-1} to +12.0 km s^{-1} (panel (c)), we see the H I corresponds to West1 H I and the H I in the north shows an intensity depression surrounding the CO, suggesting a physical association with the CO.

In the other extreme velocity range from -45.0 km s^{-1} to -25.0 km s^{-1} (panel (d)) we find the main peak at $(l, b) \sim (87°, -38°)$ shows an elongation similar to West2 H I. The H I

may be possibly linked with West2, while it was not included in the present analysis.

We summarize the above that the H I in the three panels (a)–(c) is likely associated with the main cloud within a volume having a size in the order of the main H I cloud, 30–40 pc, at a distance of 150 pc.

APPENDIX B

τ_{353}(main), which is the main component of τ_{353}, is calculated as follows.

1. First we use slope derived by least-squares fits between $W_{\rm H\,I}$ and τ_{353} by linear regression for $T_{\rm d} > 21.5$ K in Figure 4(b).
2. By using the slope derived from (1) τ'_{353} is calculated by $\tau'_{353} = \tau_{353} - W_{\rm H\,I}\,(V_{\rm LSR} < -25\,{\rm km\,s^{-1}}, +12\,{\rm km\,s^{-1}} < V_{\rm LSR})/({\rm slope})$.
3. We estimate a new slope again by the same manner as (1) between $W_{\rm H\,I}$(main) and τ'_{353}.
4. τ''_{353} is calculated by the same manner as (2) but by using τ'_{353} and the slope derived by (3).
5. We iterate (3) and (4) until the value of the slope becomes converged.

After five iterations the best estimate of the slope k converged to 8.34×10^7 K km s^{-1} with the relative variation less than 10^{-4}.

REFERENCES

Abdo, A. A., Ackermann, M., Ajello, M., et al. 2011, ApJL, 733, L26
Bell, T. A., Roueff, E., Viti, S., & Williams, D. A. 2006, MNRAS, 371, 1865
Bertsch, D. L., Dame, T. M., Fichtel, C. E., et al. 1993, ApJ, 416, 587
Blitz, L., Fukui, Y., Kawamura, A., et al. 2007, Protostars and Planets V, ed. B. Reipurth, D. Jewitt, & K. Keil (Tucson, AZ: Univ. of Arizona Press), 81
Bolatto, A. D., Wolfire, M., & Leroy, A. K. 2013, ARA&A, 51, 207
Calabretta, M. R., Staveley-Smith, L., & Barnes, D. G. 2014, PASA, 31, 7
Castets, A., Duvert, G., Dutrey, A., et al. 1990, A&A, 234, 469
Dickey, J. M. 2010, Planets, Stars and Stellar Systems, Vol. 5: Galactic Structure and Stellar Populations, ed. T. D. Oswalt & G. Gilmore (Berlin: Springer)
Dickey, J. M., & Lockman, F. J. 1990, ARA&A, 28, 215
Dickey, J. M., McClure-Griffiths, N. M., Gaensler, B. M., & Green, A. J. 2003, ApJ, 585, 801
Draine, B. T. 2011, Physics of the Interstellar and Intergalactic Medium (Princeton, NJ: Princeton Univ. Press)
Emerson, D. T., & Graeve, R. 1988, A&A, 190, 353
Fixsen, D. J. 2009, ApJ, 707, 916
Fukuda, T., Yoshiike, S., Sano, H., et al. 2014, ApJ, 788, 94
Fukui, Y. 2013, in Astrophysics and Space Science Proc. 34, Second Session of the Sant Cugat Forum on Astrophysics, ed. D. F. Torres & O. Reimer (Berlin: Springer), 249
Fukui, Y., & Kawamura, A. 2010, ARA&A, 48, 547
Fukui, Y., Sano, H., Sato, J., et al. 2012, ApJ, 746, 82
Fukui, Y., Torii, K., Onishi, T., et al. 2014, ApJ, in press (arXiv:1403.0999v1)
Gillmon, K., Shull, J. M., Tumlinson, J., & Danforth, C. 2006, ApJ, 636, 891
Gir, B.-Y., Blitz, L., & Magnani, L. 1994, ApJ, 434, 162
Glover, S. C. O., & Mac Low, M.-M. 2011, MNRAS, 412, 337
Goldsmith, P. F., Li, D., & Krčo, M. 2007, ApJ, 654, 273
Górski, K. M., Hivon, E., Banday, A. J., et al. 2005, ApJ, 622, 759
Grenier, I. A., Casandjian, J.-M., & Terrier, R. 2005, Sci, 307, 1292
Hartmann, L., Ballesteros-Paredes, J., & Bergin, E. A. 2001, ApJ, 562, 852
Heiles, C., & Troland, T. H. 2003, ApJ, 586, 1067
Hollenbach, D. J., Werner, M. W., & Salpeter, E. E. 1971, ApJ, 163, 165
Ichiki, K., Kaji, R., Yamamoto, H., Takeuchi, T. T., & Fukui, Y. 2014, ApJ, 780, 13
Inoue, T., & Inutsuka, S.-i. 2012, ApJ, 759, 35
Kalberla, P. M. W., & Kerp, J. 2009, ARA&A, 47, 27
Kawamura, A., Onishi, T., Yonekura, Y., et al. 1998, ApJS, 117, 387
Lee, M.-Y., Stanimirović, S., Douglas, K. A., et al. 2012, ApJ, 748, 75
Liszt, H. 2001, A&A, 371, 698
Magnani, L., Blitz, L., & Mundy, L. 1985, ApJ, 295, 402
Peek, J. E. G., Heiles, C., Douglas, K. A., et al. 2011, ApJS, 194, 20
Planck Collaboration. 2013, *Planck* Explanatory Supplement (Public Release 1; Noordwijk: ESA), http://wiki.cosmos.esa.int/planckpla/index.php/Main_Page
Planck Collaboration, Abergel, A., Ade, P. A. R., et al. 2011a, A&A, 536, A24
Planck Collaboration, Ade, P. A. R., Aghanim, N., et al. 2011b, A&A, 536, A19
Planck Collaboration, Ade, P. A. R., Aghanim, N., et al. 2011c, A&A, 536, A23
Planck Collaboration, Ade, P. A. R., Aghanim, N., et al. 2011d, A&A, 536, A22
Planck Collaboration, Abergel, A., Ade, P. A. R., et al. 2011e, A&A, 536, A21
Planck Collaboration, Abergel, A., Ade, P. A. R., et al. 2011f, A&A, 536, A25
Planck Collaboration, Abergel, A., Ade, P. A. R., et al. 2014a, A&A, in press (arXiv:1312.1300v5)
Planck Collaboration, Abergel, A., Ade, P. A. R., et al. 2014b, A&A, 566, A55
Rachford, B. L., Snow, T. P., Destree, J. D., et al. 2009, ApJS, 180, 125
Reich, P., & Reich, W. 1986, A&AS, 63, 205
Reich, W. 1982, A&AS, 48, 219
Sato, F., & Fukui, Y. 1978, AJ, 83, 1607
Strasser, S., & Taylor, A. R. 2004, ApJ, 603, 560
Tachihara, K., Toyoda, S., Onishi, T., et al. 2001, PASJ, 53, 1081
Welty, D. E., Hobbs, L. M., Penprase, B. E., & Blitz, L. 1989, ApJ, 346, 232
Wolfire, M. G., Hollenbach, D., & McKee, C. F. 2010, ApJ, 716, 1191
Wolfire, M. G., Hollenbach, D., McKee, C. F., Tielens, A. G. G. M., & Bakes, E. L. O. 1995, ApJ, 443, 152
Yamamoto, H., Kawamura, A., Tachihara, K., et al. 2006, ApJ, 642, 307
Yamamoto, H., Onishi, T., Mizuno, A., & Fukui, Y. 2003, ApJ, 592, 217
Yonekura, Y., Dobashi, K., Mizuno, A., Ogawa, H., & Fukui, Y. 1997, ApJS, 110, 21